CrystEngComm

PAPER

View Article Online
View Journal | View Issue

Cite this: *CrystEngComm*, 2018, **20**, 4804

Improved conductivity of a new Co(II)-MOF by assembled acetylene black for efficient hydrogen evolution reaction†

Wei Zhou,[a] Ya-Pan Wu, *[a] Xiao Wang,[a] Jun-Wu Tian,[a] Dan-Dan Huang,[a] Jun Zhao,[a] Ya-Qian Lan[b] and Dong-Sheng Li *[a]

Received 4th June 2018,
Accepted 12th July 2018

DOI: 10.1039/c8ce00921j

rsc.li/crystengcomm

Metal–organic frameworks (MOFs) incorporating different metal nanoparticles or conductive additives are expected to possess desirable catalytic performance. Herein, we report a novel 3D microporous Co(II)-MOF, $[Co_{1.5}(TTAB)_{0.5}(4,4'\text{-bipy})(H_2O)]$ (denoted **CTGU-9**), based on 3,4,5-tricarboxylic-(3′,4′,5′-tricarboxylazophenyl)benzene (H_6TTAB) and 4,4′-bipyridine (4,4′-bipy) ligands. To improve electrical conductivity, a series of composites was integrated by the assembly of **CTGU-9** and acetylene black (**AB**), and shows distinct electrocatalytic activity for the hydrogen evolution reaction (HER). Strikingly, the **AB&CTGU-9 (3 : 4)** composite exhibits superior HER performance with a very favorable onset potential of 98 mV, an overpotential of 128 mV at 10 mA cm^{-2}, a small Tafel slope of 87 mV dec^{-1} and long-term stability of at least 21 h. These results indicate that the integration of MOFs with conductive cocatalysts could produce an effective candidate electrocatalyst for HER. Additionally, the gas sorption behavior for N_2, CO_2, and CH_4 is also investigated.

Introduction

The electrocatalytic water splitting reaction has been proven to be an effective strategy for countering the shortfall in energy production.[1,2] Hydrogen is a clean and promising fuel and a potential substitute for petroleum resources. The search for efficient electrocatalysts for the hydrogen evolution reaction (HER) is of great significance.[3–6] Pt or Pt-based materials are the best electrocatalysts for HER. However, due to their high cost and low abundance, they are poorly suited to large-scale application.[7–10] Therefore, the exploration of high-efficiency, low-cost, easily synthesized non-noble metal catalysts is important.

Metal–organic frameworks (MOFs)-based electrocatalysts for HER have been widely explored. Generally, these electrocatalysts can be constructed by (i) using MOFs as precursors to synthesize metal, metal oxide, transition metal phosphide (TMP), and transition metal sulfide (TMS) nanomaterials;[11–13] (ii) exploiting pristine MOFs to catalyze the cracking of water into hydrogen through unsaturated metal atoms and the coupling effect;[14–17] (iii) synthesizing polyoxometalate (POM)-based MOFs to combine the redox nature of the POM moiety and the porosity of a MOF structure;[18–21] or (iv) developing MOFs as a carrier to entrap Pt or Mo-based composites through confinement effects.[22–24] Nevertheless, the poor electrical conductivity of MOFs limits their application in electrocatalysis for HER.[25] However, whether being chosen as an intrinsic catalyst or as a catalyst carrier or precursor, they still have the limits of poor conductivity and low active area. Thus, combining the abundant active area of MOFs with superior conductivity could be an effective strategy to attain better electrocatalytic performance.[26]

In our previous work, we found that the HER activity of 2D layered structure or 3D compact MOFs could be enhanced *via* the synergistic effect of MOFs and conducting cocatalysts.[27] Herein, a new 3D microporous Co(II)-MOF, $[Co_{1.5}(TTAB)_{0.5}(4,4'\text{-bipy})(H_2O)]$ (denoted **CTGU-9**), has been prepared and characterized. This compound features a 3D network with the (4,4,8)-c net topology. **CTGU-9** possesses higher intake capacity for CO_2 (21.637 cm^3 g^{-1}) than for CH_4. Additionally, by using a facile mechanical grinding method, a series of composites containing **CTGU-9** and acetylene black (**AB**) have been fabricated and examined in the electrocatalytic process for HER. Promisingly, the **AB&CTGU-9 (3 : 4)** composites exhibit excellent performance towards HER and demonstrate a low onset potential of 98 mV, an overpotential of 128 mV at 10 mA cm^{-2}, a small Tafel slope of 87 mV dec^{-1}

[a] *College of Materials & Chemical Engineering, Key Laboratory of Inorganic Nonmetallic Crystalline and Energy Conversion Materials, China Three Gorges University, Yichang, 443002, China. E-mail: wyapan2008@163.com, lidongsheng1@126.com; Fax: +86 717 6397506*

[b] *School of Chemistry and Materials Science, Nanjing Normal University, Nanjing, 210046, China*

† Electronic supplementary information (ESI) available. CCDC 1583330. For ESI and crystallographic data in CIF or other electronic format see DOI: 10.1039/c8ce00921j

and also long-term stability. More importantly, the easy synthesis method of the hybrid MOF-composite materials, which combine abundant active sites and high conductivity, could be a promising strategy to achieve high performance electrochemical materials.

Results and discussion

Crystal structure of CTGU-9

Single-crystal X-ray diffraction analysis shows **CTGU-9** is a 3D microporous framework. The asymmetric unit contains one and a half Co^{2+} ions, half of a fully-deprotonated $TTAB^{6-}$, one 4,4′-bipy ligand and one coordinated water molecule. As is shown in Fig. 1a, Co1 is ligated by six-coordination by two O atoms (O1, O1#1) of two $TTAB^{6-}$ carboxylate groups, two O atoms (O2, O2#1) of coordinated water molecules, and two N atoms (N1, N1#) of two different 4,4′-bipy ligands. Co2 adopts tetrahedral geometry and is coordinated by three O atoms (O4#3, O6 and O6#2) of three $TTAB^{6-}$ carboxylate groups, and one N atom (N2) of one 4,4′-dipyridyl molecule. In **CTGU-9**, the H_6TTAB ligands are completely deprotonated and bound to eight Co^{II} atoms with a μ_8-bridging coordination mode, forming a 3D framework. Finally, the 4,4′-bipy linkers ensure the necessary metal coordination numbers under the given system as well as stabilizing the 3D network (Fig. S2†) and furnishing the resulting 3D coordination porous networks (Fig. 1b and c). The total accessible volume of the two compounds is *ca.* 21.5%, which was calculated by using the PLATON program. A topological calculation using the TOPOS software suggests that such a subnet possesses a (4,4,8)-c net topology (Fig. 1d).

Gas sorption properties

CTGU-9 has two dimensional (2D) rectangle shaped channels with dimensions of approximately 13.27 Å × 11.03 Å along the *a* axis (Fig. 1b) and another channel along the *b* axis (Fig. S2†). Additionally, the X-ray powder diffraction (PXRD) patterns taken after the gas sorption experiments are shown in Fig. 3 (blue line), revealing the frameworks did not collapse. The BET study (by nitrogen sorption at 77 K) of **CTGU-9** shows promisingly high porosity. As shown in Fig. 2b, the experimental results display typical type I behavior, a characteristic of microporous materials. The maximum intake of N_2 at 1 bar for **CTGU-9** is 54.162 $cm^3\ g^{-1}$ (STP). The BET surface area for **CTGU-9** is estimated to be 168.08 $m^2\ g^{-1}$. The pore-size distributions from the analysis of the N_2 isotherm at 77 K by using the Horvath–Kawazoe (HK) method suggest that the effective pore diameter for desolvated **CTGU-9** is 1.9845 nm (Fig. 2). To fully explore the permanent microporosity of the frameworks, the CH_4 and CO_2 adsorption were also tested (Fig. 2c and d). The maximum intake of CO_2 and CH_4 at 1 bar for **CTGU-9** is 21.637, 4.021 $cm^3\ g^{-1}$ (STP), respectively. We propose that the unique pore structure promotes electrolyte ingress and accommodation of large volume changes.[25]

FT-IR, PXRD, TEM and thermal analysis

The as-prepared **CTGU-9** was also monitored by FTIR spectroscopy, PXRD, and thermogravimetric analysis (TGA). The characteristic absorption bands are mainly attributed to the stretching vibrations of carboxylate groups. As is shown in Fig. S1,† the absorption bands appearing at 3500 cm^{-1} and 3100 cm^{-1} are assigned to the O–H stretching vibrations of free lattice water and coordinated water molecules for **CTGU-9**, respectively. The peaks at 1590 and 1456 cm^{-1} are attributed to the asymmetric and symmetric stretching vibrations of C═O, respectively. Compared with the H_6TTAB carboxyl groups (1716 cm^{-1}), the lower wavenumber of C═O implies coordination between carboxyl groups and Co^{2+} ions. The PXRD patterns were recorded to examine the phase purity of **CTGU-9** and the change of the structure of the samples before and after electrocatalysis. The experimental patterns are in good agreement with the simulated patterns from crystal diffraction data, indicating the phase purity of the as-synthesized products. Additionally, the PXRD pattern of

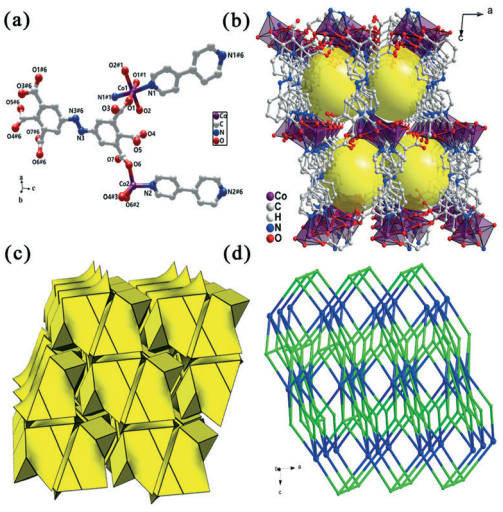

Fig. 1 (a) Coordination environments of Co(II) ions in **CTGU-9**; (b) the 3D frameworks of **CTGU-9**; (c) tiling illustration; (d) the (4,4,8)-c net topology.

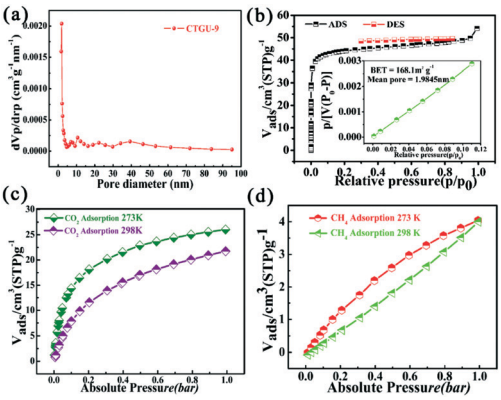

Fig. 2 (a) Pore size distributions of **CTGU-9**; (b–d) N_2, CO_2 and CH_4 sorption isotherms for **CTGU-9** at 77 K, 273 K and 298 K.

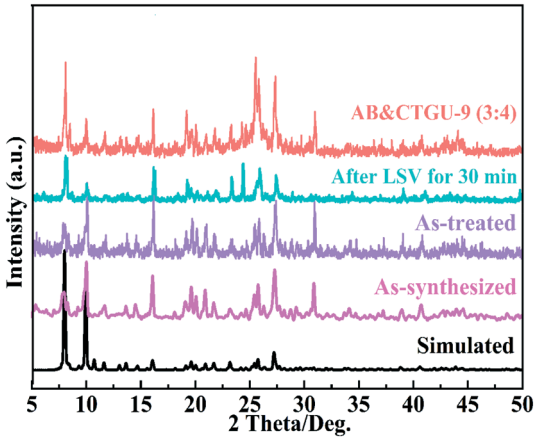

Fig. 3 The PXRD patterns of **CTGU-9**: simulated, experimental, after gas sorption and after characterization by LSV for 30 min.

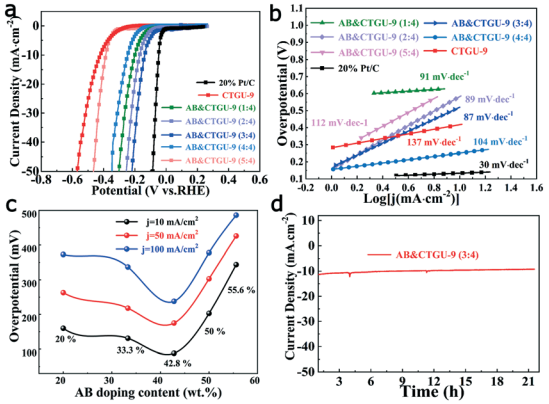

Fig. 4 (a) Polarization curves and (b) Tafel plots of **AB**, **CTGU-9** and **AB&CTGU-9** composites; (c) overpotential at current densities of 10, 50 and 100 mA cm^{-2} for **CTGU-9** with different **AB** doping contents; (d) time dependent current density curve of **AB&CTGU-9 (3 : 4)** under a static overpotential of −128 mV *vs.* RHE.

CTGU-9 after being characterized by linear sweep voltammetry (LSV) for 30 min is also in good agreement with the experimental and synthesized patterns. As is shown in Fig. 3, the **AB&CTGU-9** pattern also matches well with the simulated pattern except for a peak at $2\theta = 25.5°$, which is attributed to the presence of **AB**. To further investigate the structural stability of **CTGU-9**, it was imaged by TEM before and after 30 min of use as a water-splitting catalyst (Fig. S6 and S7†). It is clear that the morphology of **CTGU-9** after catalysis was not changed significantly. Those results strongly reveal the stability of **CTGU-9**. The TGA diagram of **CTGU-9** was recorded in the temperature range of 30–800 °C (Fig. S3†). The TGA curve of **CTGU-9** shows two main steps of weight loss. The first weight loss of 10.05% corresponds to the loss of coordinated water molecules. The second weight loss of 63.89% between 300 and 540 °C is attributed to the loss of the ligand composite (calc. 65.58%). The final residues are composed of metal oxide.

Electrocatalytic properties

The pure **CTGU-9** and series of composites fabricated from **AB** and **CTGU-9** were investigated as electrocatalysts for the HER. Note that none of the polarization curves are corrected for IR loss. The electrocatalysts were examined by modifying the samples onto a glassy carbon electrode (GCE) using a three electrode system in 0.5 M H_2SO_4.

The cyclic voltammetry (CV) and LSV polarization curves were obtained to give a preliminary assessment of the materials' electrocatalytic activity. The Tafel slope for commercial 20% Pt/C was 30 mV dec^{-1}, in agreement with values reported in the literature (Fig. 4a).[28–30] As is well known, the unmodified GCE shows poor HER activity. However, the **CTGU-9**-modified GCE reached a large current density of 10 mA cm^{-2} at an overpotential of 424 mV and positive onset potential of 321 mV (Fig. 4a and Table 1). These small values of overpotential and onset potential indicate that **CTGU-9** possesses good HER catalytic activity. In order to enhance the conductivity of the pure Co(II)-MOF, for comparison, new composite materials made from **CTGU-9** and **AB** were also studied. As shown in Fig. 4a, the samples with different additive amounts of **CTGU-9** show an enhanced electrocatalytic activity. The HER kinetics of the different catalysts was also evaluated by Tafel plots. As the content of **AB** was increased, the corresponding overpotential and Tafel slope decreased. It was found that the **AB&CTGU-9 (3 : 4)** exhibited optimal HER performance among all samples, with a positive onset potential of 98 mV, an overpotential of 128 mV and a small Tafel slope of 87 mV dec^{-1}, the HER reaction process take place *via* the Volmer–Heyrovsky mechanism (Fig. 4b). Meanwhile, when the amount of **AB** is 42.8%, the overpotential is minimized (Fig. 4c). The relationship between overpotential and **AB** additive amount reveals that adding a suitable content of **AB** can not only improve the conductivity of the AB&MOF composite (in agreement with the electrochemical impedance spectroscopy (EIS) result shown in Fig. S6†) but also enhance the electrocatalytic activity of the pure Co(II)-MOF. Moreover, the current density *versus* time (*i*–*t*) curve for **AB&CTGU-9 (3 : 4)** at a current density of 10 mA cm^{-2} reveals the catalyst retains long-term stability for at least 21 h (Fig. 4d). Additionally, as is shown in Fig. S5,† the polarization curve of **AB&CTGU-9 (3 : 4)** shows very little change *versus* the original curve even after 2000 cycles, which demonstrates its good stability during the electrocatalytic reaction. To explore the acid durability of the catalysts before and after catalysis, we tested the **CTGU-9** samples after LSV for 30 min. The main characteristic peaks after catalysis showed no obvious change. This result also provides evidence for the stability of **CTGU-9**.

The electrochemical double-layer capacitance (C_{dl}) was assessed to explore the electrochemically active surface area, where no apparent faradaic processes occurred.[30] CV was carried out at rates varying from 20 to 500 mV S^{-1} over a potential range of 0.21–0.31 V *vs.* RHE (Fig. 5). The **AB** showed a low C_{dl} of 0.040 mF cm^{-2}, while the **CTGU-9** showed a C_{dl} of 0.249 mF cm^{-2}. Meanwhile, the C_{dl} value of **AB&CTGU-9 (3 : 4)**

Table 1 Comparison of catalytic parameters of **CTGU-9** with other reported HER catalysts

Catalysts	Onset potential [mV]	Tafel slope [mV dec^{-1}]	η_{10}[a] [mV]	j_0[b] [A cm^{-2}]	Ref.
20% Pt/C	*Ca.* 0	30	40	1.71×10^{-4}	This work
CTGU-9	321	137	424	9.04×10^{-6}	
AB&CTGU-9 (1 : 4)	129	91	200	1.62×10^{-5}	
AB&CTGU-9 (2 : 4)	108	89	171	5.81×10^{-5}	
AB&CTGU-9 (3 : 4)	98	87	128	3.38×10^{-4}	
AB&CTGU-9 (4 : 4)	176	104	244	2.89×10^{-4}	
AB&CTGU-9 (5 : 4)	299	112	384	1.93×10^{-4}	
Cu-MOF	202	135	369	3.91×10^{-4}	15
NENU-501	304	137	392	2.51×10^{-4}	21
NENU-499	45	122	570	4.23×10^{-4}	
NENU-5	518	94	585	4.90×10^{-4}	
HKUST-1	612	127	691	5.65×10^{-4}	

[a] Represents the overpotential (η). [b] Represents the exchange current density. The onset potential is the overpotential at the corresponding current density of 1 mA cm^{-2}.

was 0.809 mF cm^{-2}, which is higher than that of both pure **AB** and **CTGU-9**, which reveals that the presence of **AB** could not only improve the electrical conductivity of **CTGU-9** but also reduce resistance to electrolyte ingress and ultimately allow the material to accommodate large volume changes while containing more active sites.

EIS was also performed to analyze the electrocatalytic kinetics on the electrode/electrolyte interface. The Nyquist plots demonstrate that **AB&CTGU-9 (3 : 4)** has smaller charge transfer resistance than **AB** and **CTGU-9**, which is consistent with the CV and LSV results (Fig. 4a and b). The R(CR)(CR) circuit model includes a solution resistance (Rs), ionic resistance (R_1) caused by the double layer capacitance, and charge transfer resistance (Rct) for the electrochemical reaction. The **AB&CTGU-9 (3 : 4)** modified electrode has an Rct of 633 Ω, which is higher than **AB** (442 Ω) and smaller than **CTGU-9** (1335 Ω) (Fig. S4†). All the data strongly confirm that **AB&CTGU-9 (3 : 4)** has the fastest electron transfer among all the catalysts during the equivalent HER process.

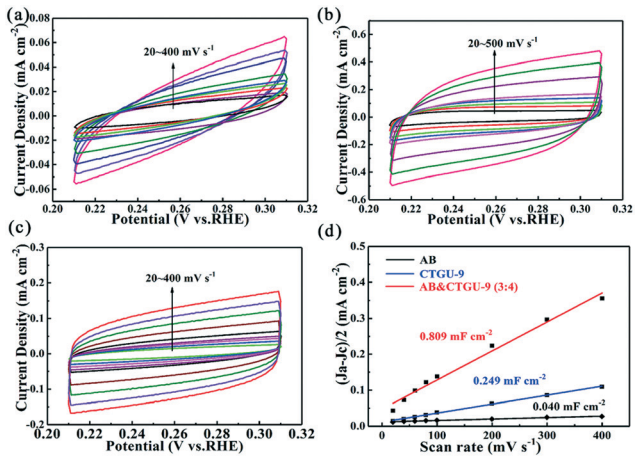

Fig. 5 (a–c) CVs of **AB**, **CTGU-9** and **AB&CTGU-9 (3 : 4)** with different rates from 20 to 500 mV s^{-1}; (d) capacitive current at 260 mV as a function of scan rate for different catalysts.

Finally, a possible mechanism of **AB&CTGU-9** for the electrocatalytic HER process is proposed as a combination of two elementary steps, where the first step is the Volmer step: $H_3O^+ + e^- \rightarrow H_{ads} + H_2O$.[31] As is shown in Fig. S8,† a proton and electron pair ($H^+ + e^-$) is introduced to the catalyst, with H^+ combining with coordinated water to form H_3O^+. Subsequently, an adsorbed hydrogen atom (H_{ads}) is formed. Due to the synergistic effect of **AB**, the **AB&CTGU-9** composite can transport more electrons than **CTGU-9** within a given time. The second step is mainly determined by the Volmer–Heyrovsky mechanism. In this situation, the Tafel ($2H_{ads} \rightarrow H_2$) process and Heyrovsky step ($H_{ads} + H_3O^+ + e^- \rightarrow H_2 + H_2O$) occur simultaneously. It is noteworthy that **CTGU-9** adopts two types of coordination modes, *i.e.* the six-coordinated active center and unsaturated coordinated active center, which synergistically catalyze the HER process.

Experimental

Materials and methods

All chemicals were purchased from commercial companies without further purification. The 3,4,5-tricarboxylic-(3′,4′,5′-tricarboxylazophenyl)benzene ligands were purchased from Jinan Camolai Trading Company. $Co(NO_3)_2 \cdot 6H_2O$ was purchased from Energy Chemical. **AB** and Nafion were purchased from Alfa Aesar Company. Powder X-ray diffraction (PXRD) was performed on a Rigaku Ultima IV diffractometer (Cu Kα radiation, λ = 1.5406 Å). FT-IR spectra (KBr pellets) were recorded on a Thermo Electron NEXUS 670 FTIR spectrometer in the range of 4000–400 cm^{-1}. Thermogravimetric (TG) curves were recorded on a NETZSCH 449C thermal analyzer with a heating rate of 10 °C min^{-1} under an air atmosphere.

X-ray crystallography

The diffraction data for **CTGU-9** were collected on a Rigaku XtaLAB diffractometer with graphite monochromatic Mo Kα radiation (λ = 0.71073 Å) and were reduced using the program CrystalClear together with an empirical absorption

correction. The crystal structure was solved through direct methods and refined based on F^2 by the full matrix least-squares method using SHELXTL. All non-H atoms were refined anisotropically. The positions of hydrogen atoms attached to carbon atoms were generated geometrically. Crystallographic data and the selected bond lengths and angles for **CTGU-9** are summarized in Tables S1 and S2.†

Synthetic procedures

A mixture of $Co(NO_3)_2{\cdot}6H_2O$ (0.05 mmol, 16.9 mg), 3,4,5-tricarboxyl-(3′,4′,5′-tricarboxylazophenyl)benzene (H_6TTAB, 0.05 mmol, 22 mg), 4,4′-bipyridine (0.05 mmol, 8 mg), 8 mL H_2O, and 0.5 mL NaOH (0.1 mol L^{-1}) was placed in a 25 mL stainless steel autoclave at 140 °C for 4 days, and cooled to room temperature. Purple bulk crystals were obtained and collected after washing with water and ethanol (yield: 52%). Elemental analysis (%): calcd for **CTGU-9** ($C_{19}H_{12}N_3O_7\ Co_{1.5}$): C: 47.28, H: 2.51, N: 8.71; found: C: 47.36, H: 2.65, N: 8.75; FTIR (KBr, cm^{-1}) (Fig. S1 ESI†): 3424 (vs), 2964 (vs), 2916 (m), 2853 (w), 2361 (m), 1618 (s), 1578 (s), 1456 (s), 1419 (s), 1383 (vs), 1045 (m), 800 (w), 723 (m), 662 (w).

Preparation of AB&CTGU-9 composite

The **AB** powder was boiled and washed in deionized water three times, and then dried in a vacuum oven. Different amounts of **AB** (10, 20, 30, 40 and 50 mg) were mixed with 40 mg **CTGU-9** powder and then ground for 30 min. The as-synthesized samples were fabricated by the above-mentioned process.

Gas sorption measurements

The N_2, CH_4 and CO_2 isotherms were collected using an ASAP 2020 surface area and pore size analyzer in a clean ultra-high-vacuum system. Approximately 200 mg of solvent-exchanged sample was loaded into the sample basket within the adsorption instrument and then degassed under dynamic vacuum at 120 °C for 6 h to obtain the fully desolvated sample. Volumetric N_2, CH_4, and CO_2 sorption measurements were performed over the pressure range 0–1 bar at 77 K for N_2, and at 273 K and 298 K for CH_4 and CO_2.

Electrochemical measurements

Electrochemical measurements were performed with a CHI 660e electrochemical workstation. All measurements were carried out in a three-electrode electrochemical cell at room temperature. A glassy carbon electrode (Ø3 mm) modified with the catalysts was used as the working electrode and a carbon rod as the counter electrode. A saturated calomel electrode (SCE) was used as the reference electrode and the potential was converted to the reversible hydrogen electrode (RHE) *via* the Nernst equation: $E_{RHE} = E_{SCE} + (0.059 \times pH) + 0.241$. The available area of the electrodes for loading the catalyst (**CTGU-9** or 20% wt Pt/C) was ~0.0706 mg cm^{-2}. Before the electrochemical measurement, the electrolyte (0.5 M H_2SO_4) was degassed by bubbling nitrogen for 30 min. The catalyst ink was prepared by dispersing a certain amount of sample into ethanol/deionized water and sonicated to ensure well-distributed dispersion. Then the catalyst ink was loaded onto a GCE of 3 mm diameter.

Conclusions

In summary, a novel 3D microporous Co(II)-MOF (**CTGU-9**) has been prepared and characterized. **CTGU-9** possesses higher intake capacities for CO_2 than for CH_4. Additionally, introducing **AB** into the porous Co(II)-MOF not only improves the conductivity of **CTGU-9** but also promotes HER performance due to the more efficient charge transport and synergistic interactions between the **AB** and Co(II)-MOF. The **AB&CTGU-9 (3 : 4)** composite possesses the optimal HER activity, with a remarkably low onset potential of 98 mV, an overpotential of 128 mV at 10 mA cm^{-2}, a small Tafel slope of 89 mV dec^{-1} and long-term stability in acidic media. The results suggest that this strategy is suitable for preparation of other highly efficient MOF-based catalysts for water splitting.

Conflicts of interest

There are no conflicts of interest to declare.

Acknowledgements

This work was supported by the NSF of China (No.: 21673127, 21671119, 51572152 and 51502155) and The Fund Program of Cultivating Outstanding Degree Theses of China Three Gorges University (No.: 2018SSPY057).

Notes and references

1 I. Roger, M. A. Shipman and M. D. Symes, *Nat. Rev. Chem.*, 2017, **1**, 0003.
2 Y. M. Shiand and B. Zhang, *Chem. Soc. Rev.*, 2016, **45**, 1529.
3 X. X. Zou and Y. Zhang, *Chem. Soc. Rev.*, 2015, **44**, 5148.
4 A. Mahmood, W. H. Guo, H. Tabassum and R. Q. Zou, *Adv. Energy Mater.*, 2016, **6**, 1600423.
5 K. Shen, X. D. Chen, J. Y. Chen and Y. W. Li, *ACS Catal.*, 2016, **6**, 5887.
6 W. Wang, X. M. Xu, W. Zhou and Z. P. Shao, *Adv. Sci.*, 2017, **4**, 1600371.
7 Y. Yan, B. Y. Xia, Z. C. Xu and X. Wang, *ACS Catal.*, 2014, **4**, 1693.
8 X. D. Wang, Y. F. Xu, H. S. Rao, W. J. Xu, H. Y. Chen, W. X. Zhang, D. B. Kuang and C. Y. Su, *Energy Environ. Sci.*, 2016, **9**, 1468.
9 J. S. Li, Y. Wang, C. H. Liu, S. L. Li, Y. G. Wang, L. Z. Dong, Z. H. Dai, Y. F. Li and Y. Q. Lan, *Nat. Commun.*, 2016, **7**, 11204.
10 J. Jiang, M. R. Gao, W. C. Sheng and Y. S. Yan, *Angew. Chem., Int. Ed.*, 2016, **55**, 1.
11 B. You, N. Jiang, M. L. Sheng, S. Gul, J. Yano and Y. J. Sun, *Chem. Mater.*, 2015, **27**, 7636.

12 J. H. Hao, W. S. Yang, Z. Zhang and J. L. Tang, *Nanoscale*, 2015, **7**, 11055.
13 L. Jiao, Y. X. Zhou and H. L. Jiang, *Chem. Sci.*, 2016, **7**, 1690.
14 A. J. Clough, J. W. Yoo, M. H. Mecklenburgand and S. C. Marinescu, *J. Am. Chem. Soc.*, 2015, **137**, 118.
15 M. Jahan, Z. l. Liu and K. P. Loh, *Adv. Funct. Mater.*, 2013, **23**, 5363.
16 Y. Gong, H. F. Shi, P. G. Jiang, W. Hua and J. H. Lin, *Cryst. Growth Des.*, 2014, **14**, 649.
17 Y. Gong, Z. Hao, J. P. Meng, H. F. Shi, P. G. Jiang, M. M. Zhang and J. H. Lin, *ChemPlusChem*, 2014, **79**, 266.
18 X. J. Kong, Z. K. Lin, Z. M. Zhang, T. Zhang and W. B. Lin, *Angew. Chem.*, 2016, **128**, 6521.
19 Y. Gong, T. Wu, P. G. Jiang, J. H. Lin and Y. X. Yang, *Inorg. Chem.*, 2013, **52**, 777.
20 W. Salomon, G. Paille, M. Mingot, P. Mialane, J. Marrot, C. R. Marchal, G. Nocton, C. M. Draznieks, M. Fontecave and A. Dolbecq, *Cryst. Growth Des.*, 2017, **17**, 600.
21 J. S. Qin, D. Y. Du, W. Guan, X. J. Bo, Y. F. Li, L. P. Guo, Z. M. Su, Y. Y. Wang, Y. Q. Lan and H. C. Zhou, *J. Am. Chem. Soc.*, 2015, **137**, 7169.
22 S. T. Wang, X. H. Gao, X. X. Hang, X. F. Zhu, H. T. Han, W. P. Liao and W. Chen, *J. Am. Chem. Soc.*, 2016, **138**, 16236.
23 Y. T. Xu, X. F. Xiao, Z. M. Ye, S. L. Zhao, R. G. Shen, C. T. He, J. P. Zhang, Y. D. Li and X. M. Chen, *J. Am. Chem. Soc.*, 2017, **139**, 5285.
24 J. Yang, F. J. Zhang, X. Wang, D. S. He, G. Wu, Q. H. Yang, X. Hong, Y. Wu and Y. D. Li, *Angew. Chem., Int. Ed.*, 2016, **55**, 1.
25 J. J. Duan, S. Chen and C. Zhao, *Nat. Commun.*, 2017, **8**, 15341.
26 L. Zhao, B. L. Dong, S. Z. Li, L. J. Zhou, L. F. Lai, Z. W. Wang, S. L. Zhao, M. Han, K. Gao, M. Lu, X. J. Xie, B. Chen, Z. D. Liu, X. J. Wang, H. Zhang, H. Li, J. Q. Liu, H. Zhang, X. Huang and W. Huang, *ACS Nano*, 2017, **11**, 5800.
27 Y. P. Wu, W. Zhou, J. Zhao, W. W. Dong, Y. Q. Lan, C. H. Sun, D. S. Li and X. H. Bu, *Angew. Chem., Int. Ed.*, 2017, **56**, 13001.
28 L. Jiao, Y. X. Zhou and H. L. Jiang, *Chem. Sci.*, 2016, **7**, 1690.
29 H. B. Zhang, Z. J. Ma, J. J. Duan, H. M. Liu, G. G. Liu, T. Wang, K. Chang, M. Li, L. Shi, X. G. Meng, K. C. Wu and J. H. Ye, *ACS Nano*, 2016, **10**, 684.
30 X. L. Wang, Y. J. Tang, W. Huang, C. H. Liu, L. Z. Dong, S. L. Li and Y. Q. Lan, *ChemSusChem*, 2017, **10**, 2402.
31 Y. X. Chen, K. N. Yang, B. Jiang, J. X. Li, M. Q. Zeng and L. Fu, *J. Mater. Chem. A*, 2017, **5**, 8187.